J Mater Sci: Mater Electron (2022) 33:25041–25052

The effect of sintering conditions on thermal stability and magnetic properties of $Ni_{0.4}Zn_{0.2}Mn_{0.4}Fe_2O_4$ ferrites

Xue-Yun Zhou[1,*], Jun Wang[2], and Li-Ling Zhou[3]

[1] School of Science, Civil Aviation University of China, Tianjin 300300, China
[2] School of Science and Jiangxi Province Key Lab of Microstructure Function Materials, Jiujiang University, Jiujiang 332005, Jiangxi, China
[3] Department of Electronics and Information, Huzhou College, Huzhou 313000, China

Received: 13 August 2022
Accepted: 22 September 2022
Published online: 8 October 2022

ABSTRACT

$Ni_{0.4}Zn_{0.2}Mn_{0.4}Fe_2O_4$ ferrites were synthesized via sol–gel auto-combustion process under different sintering conditions. By supplying N_2 flux or high sintering temperature, pure NiZnMn complex ferrites can be obtained, and the magnetic properties are also optimized. Cooling in vacuum after annealing in air has the best effect on the improvement of the magnetic properties. Its initial permeability is twice that of the sample cooled in air, up to 95. Its saturation magnetization and coercivity are 76 emu/g, 55Oe, respectively, which have big particle size and more Fe ions at B-site. The average thermal coefficient of the samples annealed at 950 °C in N_2 atmosphere is less than 0, maybe due to the compensation of Fe^{2+}. And its thermal stability and Curie temperature are the highest. It is worthy noticed that the Curie temperature of all samples is higher than 315 °C and the cut-off frequency is between 38 and 220 MHz, indicating that these samples can be used in short-wave antenna, high frequency inductor core, filter inductor core, and pulse transformer core, etc.

1 Introduction

Spinel ferrites are widely used in aerospace area, transportation region, medical field, electric power and normal domestic appliance because of excellent soft magnetic and high frequency properties with high resistivity(up to $10^8\Omega$ m), low residual magnetic flux density and coercivity, excellent chemical and temperature stability [1]. It is well known that MnZn ferrites exhibit high initial permeability (μ_i) due to magnetocrystalline anisotropy constant (K) close to zero and was used in low frequency range. They need to be prepared in reducing atmosphere [2]. There are lots of reports about the preparation of pure Mn-containing ferrites and improvement of magnetic properties. Guohua Wu [3] prepared pure spinel $Mn_{0.67}Zn_{0.21}Fe_{2.12}O_4$ ferrites at 1150° C in controlled partial pressure of oxygen for 5 h. Its core loss is ultra-low at high frequency. The resonant frequency is about 8 MHz and can be enhanced by adding nano-$BaTiO_3$. Akhlaq Hussain [4] prepared pure Co_2O_3 and SnO_2 doped $Mn_{0.705}Zn_{0.165}Fe_{2.13}O_4$

Address correspondence to E-mail: xyz8301@163.com

https://doi.org/10.1007/s10854-022-09211-8

spinel ferrites at 1170 °C in controllable oxygen's partial pressure for 4 h, which have high initial permeability (μ_i = 600) and can be for applications at 3-5 MHz. Shilpa V. Bhandare [5] found that in air atmosphere, it is easy to obtain single CoMnZn ferrite phase when Zn content and the annealing temperature are low. Zhanyuan Xu [6] obtained pure $Mn_{0.5}Zn_{0.5}Fe_2O_4$ ferrites after calcining at 1060 °C -1080 °C. Some second phases (Mn_2O_3 and α-Fe_2O_3) appear when sintering temperature is below 1060° C, and the maximum value of the saturation magnetization is 53.49 emu/g in the sample annealed at 1060 °C. S. Mallesh [7] demonstrated that there were no impurity phases in $Mn_xZn_{1-x}Fe_2O_4$ with $x < 0.8$ in an air atmosphere of 1200 °C. Ar gas treatment and liquid nitrogen quenching are beneficial to form pure MnZn ferrites. At the same time, the crystalline structure and magnetic properties were also improved.

Proper doping can enhance the application frequency. NiZn ferrites have high Curie temperature and cut-off frequency. For example, JinAh Hwang [8] prepared the toroidal $Ni_{1-x}Zn_xFe_2O_4$ (x = 0.5, 0.6, 0.7)ferrite at 1250 °C for 2 h in air and found that the cut-off frequency is about 20 MHz. The real magnetic permeability (μ') increased with increasing Zn content, showing μ' = 217 for x = 0.7. So, NiZnMn composite ferrites are expected to have high cut-off frequency and initial permeability. However, this is not the fact. U.B. Gawas [9] reported that the existence of a second phase in the $Zn_{0.5}Mn_{0.5}Fe_2O_4$ ferrite annealed at 1100 °C, while all $Ni_{1-x}Zn_{0.5}Mn_xFe_2O_4$(-x = 0–0.5) ferrites annealed at 1250 °C have single spinel structure with high resistivity (10_7-$10^8\Omega$ cm). The maximum initial permeability was about 280 in the sample with x = 0.2. The curie temperature can be adjusted from 320 to 360 °C. But their cut-off frequency is not higher that reported in reference 8.

By summary, it is easy for the second phase to appear in Mn-containing ferrites. High annealing temperature and protective gas treatment can help to form pure Mn-containing ferrite and improve their magnetic properties. The most NiZnMn ferrites were prepared by annealing in air at high temperature. In this paper, $Ni_{0.4}Zn_{0.2}Mn_{0.4}Fe_2O_4$ formula with less Zn content was selected to obtain high cut-off frequency and high-permeability. Various heat treatment methods are used. Except for N_2 atmosphere treatment and high-temperature sintering, sintering at high temperature + cooling in vacuum is used to further improve the magnetism of NiZnMn ferrite. Their effects on the structure, magnetic properties and thermal stability of $Ni_{0.4}Zn_{0.2}Mn_{0.4}Fe_2O_4$ ferrites are compared. The Sol–Gel auto-combustion method is used to prepare the sample. Because in this method, component adjustment is easy and the products have high homogeneity [10].

1.1 Experiments

The $Ni_{0.4}Zn_{0.2}Mn_{0.4}Fe_2O_4$ ferrites were prepared via the Sol–Gel auto-combustion method. The raw materials includes analytically pure $Ni(NO_3)_2{\cdot}6H_2O$, Zn $(NO_3)_2{\cdot}6H_2O$, Mn $(NO_3)_2{\cdot}4H_2O$, Fe $(NO_3)_3{\cdot}9H_2O$, citric acid, and ammonia. Detailed synthesis process of gel was reported in an earlier work [11] and process flow diagram was shown in Fig. 1. The powders obtained after auto-combustion at 200 °C were mixed with polyvinyl alcohol (PVA) binder. Then the ground mixture was pressed into toroidal specimens under a pressure of 20 MPa. Finally, these toroids were sintered in air at 950 °C for 2 h, named Air950; in air at 1200 °C for 2 h, named Air1200; with N_2 at 950 °C for 2 h, named $N_2$950; in air at 1200 °C for 2 h and then cooled in vacuum from 1200 °C to room temperature, named Vac1200, respectively. The heating rate is 2 °C/min.

Thermogravimetric (TG) and differential thermal (DSC) analysis were performed with heating rate of 10 °C/min in air atmosphere using NETZSCH STA 449F3. X-ray diffraction (XRD) studies were performed by D8 ADVANCE to determine the crystal structure of the samples; Fourier transforms infrared spectra (FTIR) were recorded in the range of 4000 cm^{-1} to 300 cm^{-1} using VERTEX70 FTIR spectrometer (Bruker); The surface morphology of the synthesized rings was analyzed by scanning electron

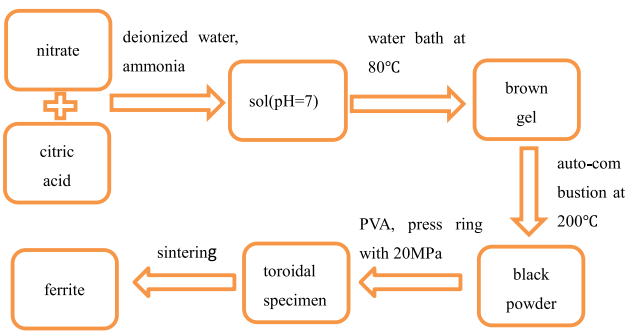

Fig.1 Preparation route of ferrite by sol–gel auto-combustion method

microscope (SEM) (VEGA), and the chemical elements of typical sample Air1200 was analyzed by energy dispersive spectrometer (EDS); The initial permeability and Curie temperature were measured with the LCR digital bridge (TH2828); The magnetic hysteresis loops of NiZnMn ferrite were measured at room temperature by the vibrating sample magnetometer (VSM) (BKT4500Z); The chemical states of the species present were determined using X-ray photoelectron spectroscopy (XPS) on thermo escalab 250XI; The real part of complex permeability (μ') was measured using a vector network analyzer (Agilent16454A) in the frequency range of 1 MHz -1 GHz under the condition that the bulks were broken and mixed with paraffin (20% mass ratio) and pressed into a toroid mold with an outer diameter of 7.0 mm and inner diameter of 3.04 mm; The temperature dependence of saturation magnetization was measured at 5000Oe using Quantum Design PPMS-9.

2 Results and discussion

Thermogravimetric (TG) and differential thermal (DSC) analysis of the powders obtained after auto-combustion at 200 °C shown in Fig. 2 was carried out in air to discuss the formation process of ferrite. The main mass loss is about 11% from RT to 367 °C with an endothermic peak at 342 °C in DSC curve. It is far less than the 40% and 60% mass loss reported by Zhanyuan Xu [6] and Prajyoti P. Gauns Dessai [12], indicating that most carbon, hydrogen and nitrogen were removed after auto-combustion to form ferrite. A mass loss of 5% from RT to 247 °C was due to the removal of adsorbed water and incompletely reacted carbon containing group. The rest of mass loss occurred due to the decomposition of remaining nitrate. From the end of nitrate decomposition to 490 °C, the increase in mass (0.7%) corresponds to an oxidative decomposition reaction of ferrite into Fe_2O_3 and Mn_2O_3. Another endothermic peak at 589 °C was observed in DSC curve, and there are other small amount of mass loss when temperature is higher than 934 °C. Other research teams also report the similar results. S. Mallesh [7] reported that mass loss corresponding to reduction processes occurs above 1000 °C. Zhongxia Duan [13] reported a mass loss from 800 to 1000 °C corresponding the formation of $Mn_xZn_{1-x}Fe_2O_4$. Zhanyuan Xu [6] observed an endothermic peak at 1000 °C due to the formation of MnZn ferrites and a mass gain at 1070 °C. These references and our data indicate that the synthesis temperature of manganese-based ferrite is about 1000 °C.

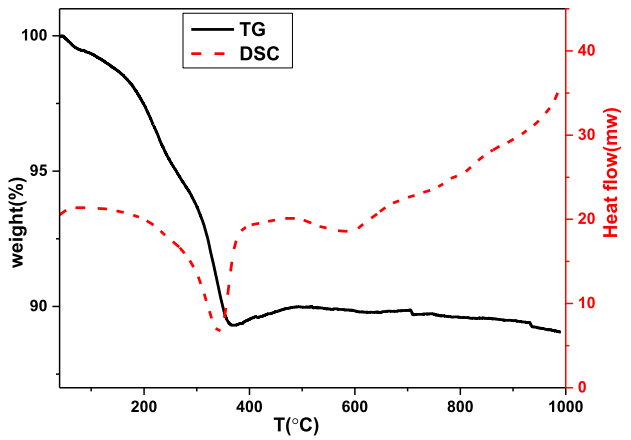

Fig. 2 TG and DSC curves performed in air of the products after auto-combustion

SEM patterns of the four samples are shown in Fig. 3a-d. It can be seen that the particles of Air950 and $N_2$950 agglomerate seriously and their shape is not clear. All ferrites sintered at 1200 °C have relatively well-defined particle shapes. The particle size ranges from a few hundred nanometers to 3um. The mean particle size of Air1200 and Vac1200 (Fig. 3e–f) reaches about 1.3 μm.

The EDS spectrum of the sample Air1200 is shown in Fig. 4. The presence of all the expected elements was confirmed, and the atomic ratio of Mn, Fe, Ni, and Zn is 0.41:2.04:0.36:0.19, which is nearly consistent with the formula.

Figure 5 presents the XPS analysis of $Ni_{0.4}Zn_{0.2}Mn_{0.4}Fe_2O_4$ samples sintered under different conditions to check the chemical states of Fe and Mn elements on the material surface. The Fe 2p spectra show two peaks for $Fe2P_{3/2}$ and $Fe2P_{1/2}$ with binding energy at 710.4 eV and 724.2 eV, respectively. In addition, two satellite peaks appear at 718.9 eV and 732.8 eV, indicating the presence of Fe^{3+} [14]. The peak shape of $Fe2P_{3/2}$ spectra was fitted using the Lorentian-Gaussian [15], which also can be divided into two peaks at 710.8 eV and 712.8 eV. Most researchers [16, 17] believe that they correspond to octahedral $Fe^{3+}(O_h)$ and tetrahedral $Fe^{3+}(T_h)$. The integrated area under each peak is a measure of the corresponding cation concentration in the measurement area [18]. The relative concentrations of

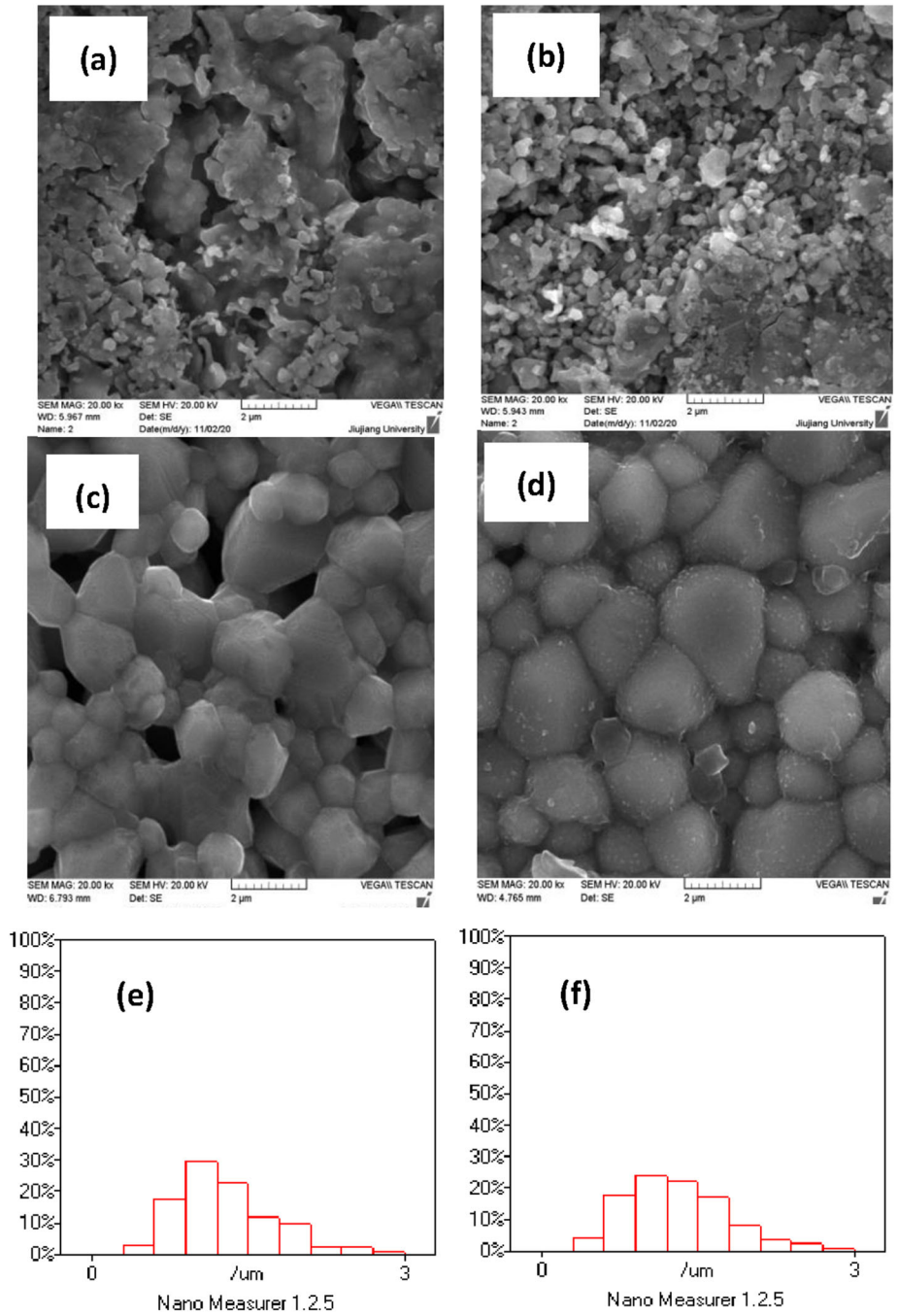

Fig.3 **a-d** SEM patterns of Air950 **a**, $N_2$950 **b**, Air1200 **c**, and Vac1200 **d**; Fig. 3 **e–f** Particle size distribution of Air1200 and Vac1200, respectively

octahedral Fe^{3+} species is 59.4%, 61.8%, and 68.5% in the samples $N_2$950, Air1200, and Vac1200, respectively.

In Fig. 5b, the binding energy of $Mn2P_{3/2}$ and $Mn2P_{1/2}$ is 641.1 eV and 652.9 eV, respectively. The same deconvolution method is used to analyze Mn2p spectra. A peak with binding energy of 639.5 eV was observed only in Vac1200, which corresponds to the characteristic peak of Mn metals. For the two fitting peaks at 640.9 eV and 642.5 eV, some researchers [19, 20] reported that they are associated with Mn^{2+} and Mn^{3+}. Other researchers [17] thought they are related to octahedral and tetrahedral Mn^{2+} species. Because the samples are sintered in air, some Mn^{2+} ions will be oxidized to high valence Mn ions. And the impurity (Mn_2O_3 detected by XRD (Fig. 5a) in the sample Air950 did not result in the appearance of new peaks in Mn 2P spectra (Fig. 4b), indicating that

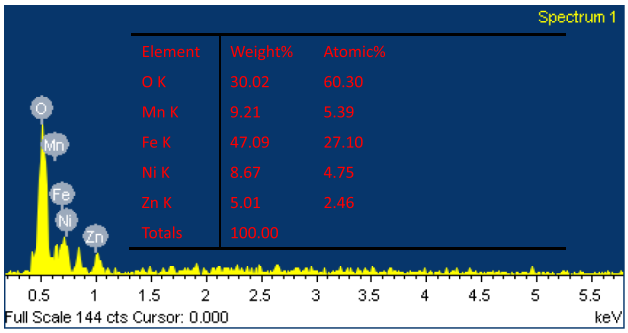

Fig.4 EDS spectrum and elemental mapping of the sample Air1200

the ions states of some Mn in ferrite are similar with them in impurities. So Mn^{2+} and Mn^{3+} coexist in the NiZnMn ferrites.

Figure 6 shows XRD patterns of $Ni_{0.4}Zn_{0.2}Mn_{0.4}Fe_2O_4$ samples annealed under different conditions. It can be seen that in the sample Air950, a small amount of impurity phases, such as Fe_2O_3 (JCPDS card no. 33–0664) or Mn_2O_3 (JCPDS card no.33–0900), are detected by XRD, which are marked by symbol * in Fig. 6. However, in the samples prepared in N_2 atmosphere or at higher temperature, the impurity phases disappear (Fig. 6b-d). The three groups of samples ($N_2$950, Air1200, and Vac1200) reveal single-phase cubic spinel structure (JCPDS card no.47–0023) with all indexed peaks.

Rietveld refinement is fulfilled using Fullprof software. The lattice parameters, bond length, and bond angle are obtained from Rietveld refinement. These results are shown in Table 1 with the fitting accuracy parameters: Bragg R-factor and χ^2. The refinement results show that Air950 contain ferrite phases with a mass fraction of 70%. From Table 1, it can be seen that the change of lattice constant (a) follows the following rules: Vac1200 > Air1200 > $N_2$950 > Air950. N.I. Abu-Elsaad [21] studied the effect of annealing temperature on structure of LiZn ferrites and found that with significant growth of crystal grains at higher annealing temperature, the lattice parameter can be enlarged by reducing surface disorder. The growth of crystal grains can be confirmed by SEM patterns (Fig. 3). In addition, the increase in the number of Mn^{2+} with a radius (0.83 Å) larger than Mn^{3+} (0.645 Å) is another reason. N_2 atmosphere, high annealing temperature and cooling in vacuum can provide an anoxic atmosphere, which is conducive to the formation of MnZn ferrite and prevent Mn^{2+} oxidation. S. Mallesh also reported [7] that MnZn ferrites with larger lattice constant when they were annealed in Ar atmosphere and quenched in liquid nitrogen.

From Table 1, the change of cation occupation with annealing condition was simply analyzed. The bond length A–O and B–O of $N_2$950 is slightly larger than that of Air950, showing that a small amount of Mn^{3+} at A-site and B-site are transformed into Mn^{2+} when the sample is annealed in N_2. The samples annealed at 1200 °C have greater bond length A–O and smaller B–O, indicating that more Mn ions occupy A-site and some Fe^{3+} ions are squeezed to B-site. Cooling in vacuum can enlarge the bond length A–O and B–O, which means more Mn^{2+}. The bond angle A–O–B and B–O–B are affected slightly by the annealing condition.

The FTIR spectra can also demonstrate these results, as shown in Fig. 7. There are two main absorption bands υ_1 and υ_2 at about 580 cm^{-1} and 400 cm^{-1}, which are corresponding to tetrahedral (A-site) and octahedral (B-site) cations [22], respectively. The position of υ_1 and υ_2 peak is shown in Table 1. υ_1 shifts gradually toward lower frequency for the four samples. It can be explained by the increase of bond length A–O (Table 1) resulting in the decrease of

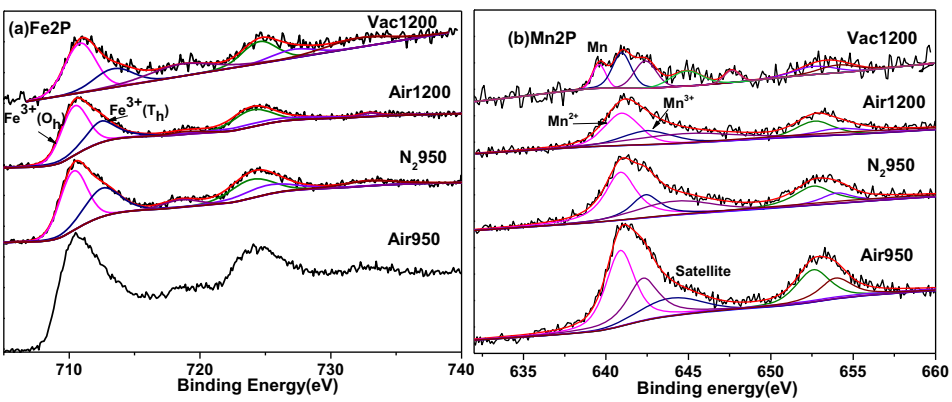

Fig.5 Fe2P (**a**) and Mn2P (**b**) XPS spectra of $Ni_{0.4}Zn_{0.2}Mn_{0.4}Fe_2O_4$ samples

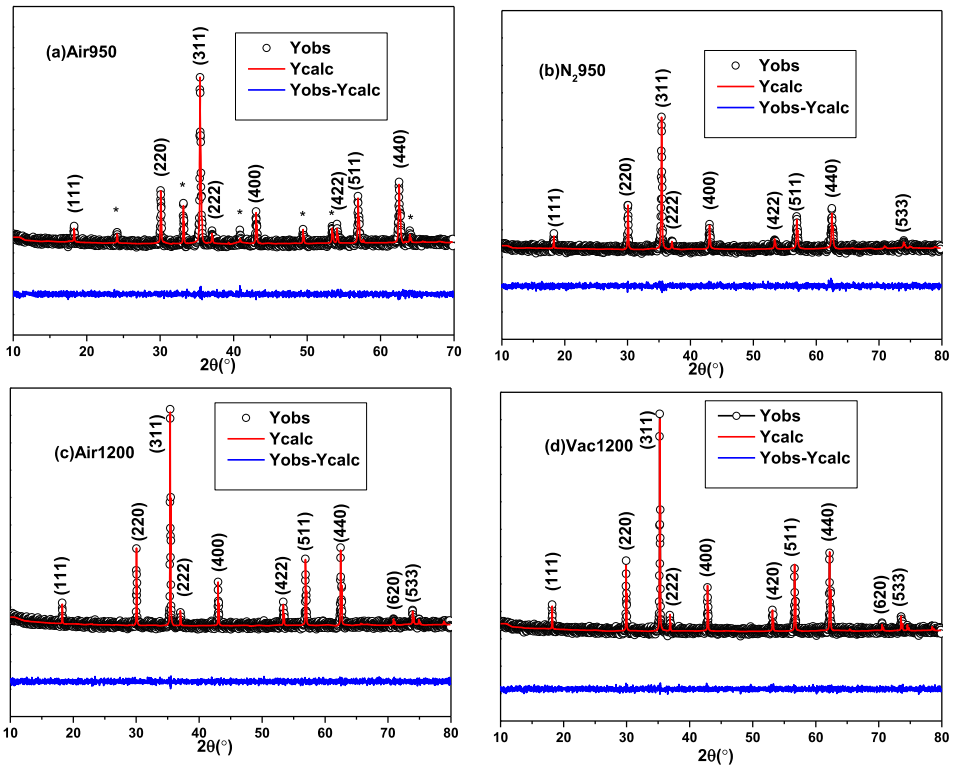

Fig.6 Rietveld refinement of XRD patterns for $Ni_{0.4}Zn_{0.2}Mn_{0.4}Fe_2O_4$ samples

Table 1 The structural parameters from Rietveld refinement and IR parameters

	a(error)(Å)	Bond length(Å)		Bond angle(°)		Bragg R-factor	χ^2	υ_1(cm^{-1})	υ_2(cm^{-1})
		A–O	B–O	A–O–B	B–O–B				
Air950	8.3967(0.0013)	1.9168	2.0437	123.0	93.2	2.38	1.23	583	400
$N_2$950	8.4010(0.0013)	1.9193	2.0439	123.0	93.2	4.01	1.20	580	401
Air1200	8.4024(0.0007)	1.9385	2.0340	122.5	93.8	3.15	1.10	577	400
Vac1200	8.4373(0.0007)	1.9509	2.0401	122.4	94.0	3.55	1.19	575	401

chemical bond strength. However, the change of the absorption band υ_2 is not obvious. U.B. Gawas [9] found that in $Ni_{0.5-x}Mn_xZn_{0.5}Fe_2O_4$ ferrites, the frequency of υ_2 did not change noticeably, because Mn substitution has hardly any effect on octahedral bond length. Yassine Mouhib [23] found no difference in absorption band υ_2 between the samples annealed at 400 °C and 500 °C because the crystallite size of the two samples is close. Obviously, here octahedral bond length and crystal size can't explain absorption band υ_2. In G.M. Shweta's paper [24], the irregular displacement of υ_2 is attributed to both reduced mass and bond length. According to spring model of atomic vibration, the absorption band is also inversely proportional to $\sqrt{m}$, in which m is the reduced

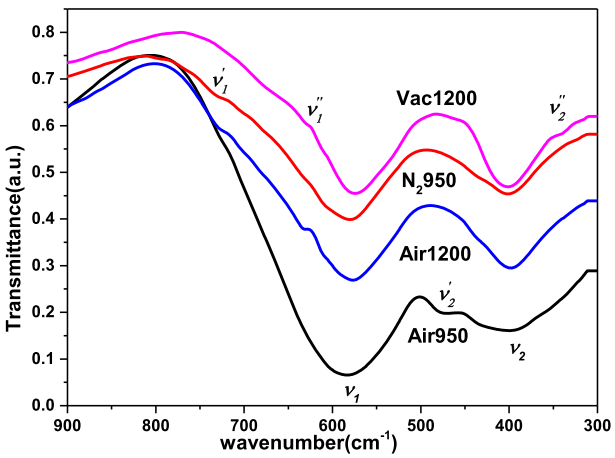

Fig. 7 FTIR spectra of all sintered samples

mass. The decrease of bond length and the increase of average mass lead to the invariance of υ_2. In the IR spectra of Air950, there is a new absorption band υ_2' at 470 cm^{-1} corresponding to Ni^{2+}–O^{2-}, which is also reported by U.B. Gawas [9]. It is because the formation of the second phase results in high nickel content in the ferrite phase. The weak peak υ_1' at 730 cm^{-1} in Air1200 and $N_2$950 can be assigned to the stretching vibration of the tetrahedral Mn^{3+}–O^{2-} bonds. Because the intensity became low, it is invisible in Air950 and Vac1200. Two weak peak υ_1'' at 633 cm^{-1} and υ_2'' at 342 cm^{-1} in Vac1200 with high Mn^{2+} content can be assigned to the stretching vibrations of the Fe^{3+} (A)–O^{2-}–Mn^{2+} (B) group.

Figure 8 shows the typical magnetic hysteresis loops of the four samples. All hysteresis loops display soft ferromagnetic behavior. The saturation magnetization (M_s) and coercive field (H_c) are presented in Table 2. It is noticed that for the four samples: Air950, $N_2$950, Air1200, and Vac1200, M_s increases in turn and H_c decreases in turn. M_s of Vac1200 is 76 emu/g, close to the value (83.14 emu/g) in $Ni_{0.55}Zn_{0.3}Co_{0.15}Fe_2O_4$ reported by Xiao-Hui Wu [25]. It is larger than that of $Mn_{0.5}Zn_{0.5}Fe_2O_4$ [6] and $Ni_{0.5}Zn_{0.5}Fe_2O_4$ [26]. Certainly, the formation of non-magnetic second phase is a reason for the worst magnetic properties of Air950. The redistribution of cations is a main factor affecting M_s as an intrinsic physical quantity. According to Neel's two sub-lattice model [27], M_s is proportional to the difference between the magnetic moment of octahedral ions (M_B) and the magnetic moment of tetrahedral ions(M_A). The Magnetic moment of Mn^{2+} is 5μ_B, larger than that of Mn^{3+} (4μ_B). According to the above cation distribution

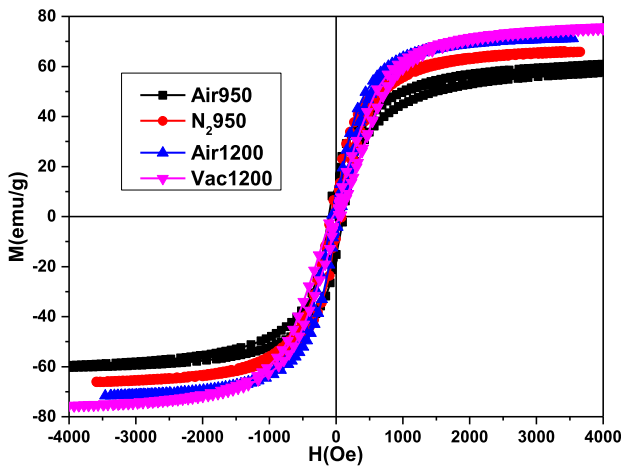

Fig. 8 The hysteresis loops of all samples

analysis, Mn^{2+} at A-site and B-site in $N_2$950, Air1200 and Vac1200 increases gradually. And after high temperature annealing, some Fe^{3+} ions (5μ_B) migrate from A-site to B-site. Other factors, such as grain integrity, can also affect the saturation magnetization of the material. Raghvendra Singh Yadav [28] and N.I. Abu-Elsaad [21] reported that with the increase of particle size (D), the development of multi-domain particles and limited number of grain boundaries can induce an increase of M_s and decrease of H_c. From Fig. 3 and Table 2, the change of saturation magnetization is consistent with that of particle size. Coercivity depends on the microstructure of the material. So the change of coercivity can be attributed to the particle size (SEM images (Fig. 3)).

The initial permeability (μ_i) is an important parameter of soft ferrite materials, which depends on the magnetization mechanism, involving domain rotation and domain wall displacement. The initial permeability is related to the intrinsic properties of ferrite as follows [4]

$$\mu_i \propto \frac{M_s^2}{K}$$

In the low frequency range (1 K-1 MHz), permeability hardly changes with frequency, showing well frequency stability and a wide application frequency range, as shown in Fig. 9. The initial permeability at 100 kHz is obtained, as shown in Table 2. Obviously, the largest μ_i is 95 in Vac1200, which is larger than the permeability of $Ni_{0.8}Zn_{0.2}Fe_2O_4$ ferrite reported by T. Jahanbin [29] and $Ni_{0.5}Zn_{0.3}Cd_{0.2}Fe_{2-x}La_xO_4$ ferrite reported by S. Ikram [30]. This value even reached the value of the samples with high Zn content annealed in air [31]. But it still much smaller than the initial permeability of MnZn ferrites [32] and NiZnMn ferrites prepared by standard solid-state reaction technology [33], shown in Table 2. The change rule of μ_i can be explained by the magnetization mechanism, which is consistent with that of M_S for the four samples. In addition, the microstructure affects the dynamic balance of magnetization, thus affecting μ_i. For Air950 and $N_2$950, the particle size is small, so the blocking effect of grain boundary on domain wall displacement increases, resulting in small μ_i. The presence of impurity for Air950 further reduces μ_i. This reduction of the permeability is thought as the reason of the improvement of cut-off frequency (f_r). From Fig. 10 and Table 2, the change rule of f_r is opposite to that of

Table 2 the magnetic parameters of $Ni_{0.4}Zn_{0.2}Mn_{0.4}Fe_2O_4$ samples and other systems

	M_s (emu/g)	H_c(Oe)	μ_i	f_r(MHz)	T_c(°C)	*Refs*
Air950	58	107	6	220	349	This work
$N_2$950	66	77	13	123	408	This work
Air1200	71	60	46	70	366	This work
Vac1200	76	55	95	38	319	This work
$Ni_{0.55}Zn_{0.3}Co_{0.15}Fe_2O_4$	83.14	13.66	48	–	–	[25]
$Mn_{0.5}Zn_{0.5}Fe_2O_4$	53.49	28.03	–	–	–	[6]
$Ni_{0.5}Zn_{0.5}Fe_2O_4$	72.07	1.85	65	–	256	[26]
Co_2O_3 and SnO_2 doped $Mn_{0.705}Zn_{0.165}Fe_{2.13}O_4$	–	–	326	21	–	[4]
$Ni_{0.8}Zn_{0.2}Fe_2O_4$	–	–	18	23	–	[29]
$Ni_{0.5}Zn_{0.3}Cd_{0.2}Fe_2O_4$	40.31	70.85	36.4	–	–	[30]
$Ni_{0.2}Zn_{0.4}Mn_{0.4}Fe_2O_4$	54	70	100	–	281	[31]
MnZn ferrite	–	–	12,254	–	124	[32]
$Ni_{0.3}Mn_{0.2}Zn_{0.50}Fe_2O_4$	–	–	677	1	179	[33]
$Ni_{0.2}Mn_{0.3}Zn_{0.5}Fe_2O_4$	65	22	362	–	277	[36]

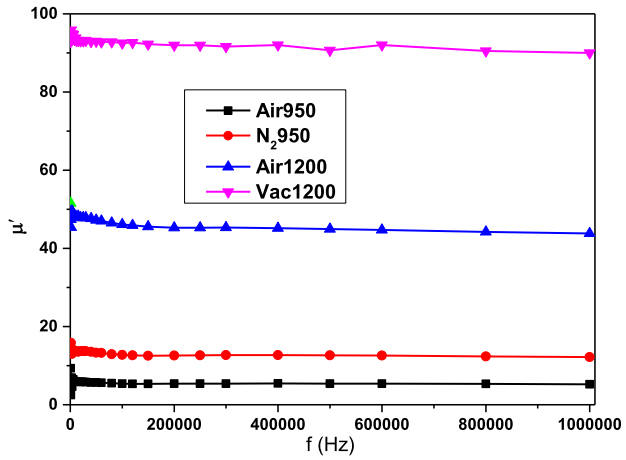

Fig. 9 The true part of permeability via frequency curves measured from 1 kHz to 1 MHz

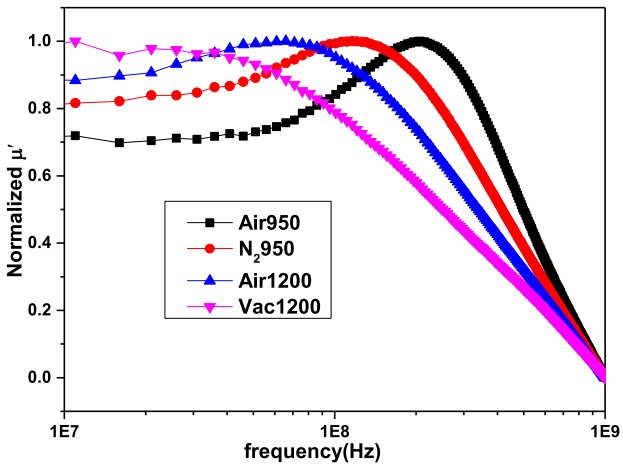

Fig. 10 The normalized true part of permeability via frequency curves of these samples

μ_i for the four samples. The cut-off frequency of Air950 is higher than 220 MHz, and the cut-off frequency of Air1200 is higher than 70 MHz. These values are higher than the reported cut-off frequency of ZnMn ferrites [4] and the NiZnMn ferrites [33].

The thermal variation of the initial permeability of the NiZnMn ferrites is donated in Fig. 11. The change of magneto-crystalline anisotropy constant K with temperature is faster than that of M_S with temperature. So there is a sharp peak near Curie temperature, corresponding to the temperature point with magneto-crystalline anisotropy constant $K = 0$. This can be confirmed by the M_S-T and μ_i –T curves, as shown in Fig. 11. With the increase of temperature, *Ms* decreases due to thermal effect. Near the Curie temperature point, M_S drops slowly to 0. However, the peak disappears in μ_i-T curves for the samples annealed at lower temperature (Air950 and $N_2$950) and the curves become more flat.

In a certain temperature interval (T_2-T_1), average thermal coefficient (α_μ) can be calculated by the equation.

$$\alpha_\mu = \frac{\mu_{T_2} - \mu_{T_1}}{\mu_{T_1}(T_2 - T_1)}$$

where μ_{T2} and μ_{T1} are the initial permeability at temperature T_2 and T_1, respectively. Between room temperature and 310 °C, α_μ is 8×10^{-4}, -5×10^{-4},

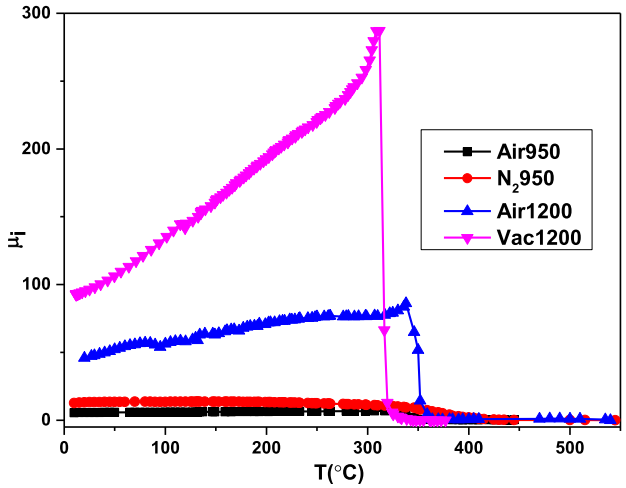

Fig. 11 The temperature dependence of the initial permeability of all synthesized samples

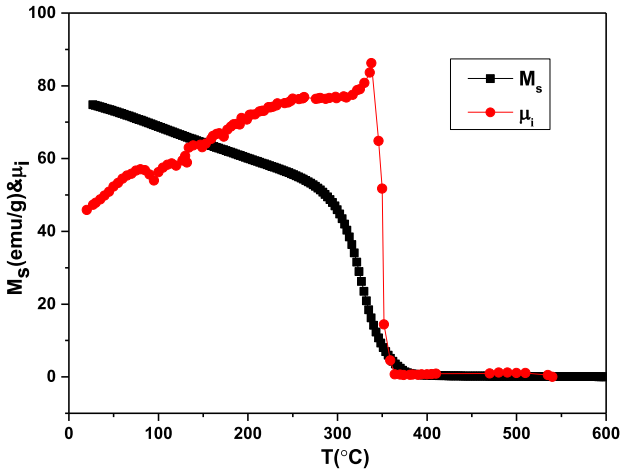

Fig. 12 M_s-T and μ_i-T curves for Air1200

2×10^{-3}, and $7 \times 10^{-3}$for Air950, $N_2$950, Air1200, and Vac1200, respectively. Obviously, the samples annealed in air (Air950, Air1200, and Vac1200) show a positive thermal coefficient of permeability. The μ_i rises with temperature, indicating a better adaptability of environment. Kaiqi Jiang [32] reported that the MnZn ferrite sintered in elevator furnace at 1380 °C for 4 h with 3.0% partial pressure of oxygen and cooled at equilibrium conditions in a N_2/O_2 atmosphere has also a positive thermal coefficient. In Ni-Zn-Me(Cu, Mn, Co, Mg, Cd, Ca) ferrites prepared by conventional ceramic processing [34] and LiZn ferrites prepared by a sol–gel auto-combustion process [21, 35], the same results was observed. Among the three samples, Vac1200 has the worst thermal stability, and Air950 has the best thermal stability. It is consistent with the microstructural variety. From Fig. 3, Vac1200 has the most uneven size distribution and the largest grains. However, the thermal coefficient of $N_2$950 is less than 0, different with other samples. The coefficient value is also the smallest. It should be due to the compensation effect of Fe^{2+} ions with positive K. In fact, Fe^{2+} ions were not detected by XPS (Fig. 5), indicating that the amount of Fe^{2+} ions is very small. Air1200 and Vac1200 with higher Mn^{2+} content has lower Fe^{2+} content, because Mn^{2+} will inhibit the formation of Fe^{2+}. So if the annealing atmosphere is well controlled when the samples are prepared at high temperature, the coefficient can also be reduced, even close to 0.

The Curie temperature (T_c) of the material is obtained by the intersection of the tangent line at the maximum slope and the temperature axis ($\mu_i = 0$), shown in Table 2. By the way, the Curie temperature obtained from Fig. 12 is consistent with that obtained from Fig. 11, which proves the correctness of the experiment. Curie temperature is an intrinsic characteristic, which is determined by the composition of ferrite. The general rule is that the stronger the superexchange interaction of magnetic ions between A sites and B sites, the higher the Curie temperature. It can be seen that the Curie temperature of all the sample is between 319 and 408 °C, higher than that of Mn-Zn ferrite whose Curie temperature is 124 °C [32], mixed $Ni_{0.5-x}Mn_xZn_{0.5}Fe_2O_4$ (x = 0.1–0.4) ferrites whose Curie temperature is about 475-675 K [36] and mixed $Ni_{0.5-x}Mn_xZn_{0.5}Fe_2O_4$ (x = 0.1–0.2) ferrites whose Curie temperature is about 235–245 °C [33]. T_c of Vac1200 is the lowest, which may be due to the increase of bond length and Mn^{2+} at A-site. It is known that the super-exchange interaction of Mn–O-Fe is smaller than Fe–O–Fe. T_c of Air950 is not high because the formation of the second phase leads to the high Zn content in ferrite composition. For $N_2$950, μ_i slowly drops to 0 near Curie temperature, which leads to higher T_c. This behavior is as if the composition of the material is uneven. It is possible that some particles contain more Mn and less Zn, while others do the opposite.

3 Conclusion

$Ni_{0.4}Zn_{0.2}Mn_{0.4}Fe_2O_4$ ferrites have been prepared by sol–gel auto-combustion method. The effect of sintering condition on the structure, thermal stability

and magnetic properties has been investigated. From above discussion, following conclusion are obtained.

1. A single spinel structure can be obtained when the samples were annealed in N_2 or at higher temperature with the increase of particle size. More Mn^{2+} ions appear and prefer to occupy A-site in the sample cooled in vacuum.

2. The magnetic properties of the samples can be explained by microstructure and distribution of cations. The specimens annealed at 1200 °C and cooled in vacuum have the best magnetic properties with the largest M_s, the lowest H_c, and the largest μ_i, because of large grains and more Fe^{3+} ions in B-site. The samples annealed at 950 °C in air have the worst magnetic properties due to the second phase and small grains.

3. The samples annealed at 950 °C in N_2 atmosphere have the excellent thermal stability, maybe due to the compensation of Fe^{2+} ions. The samples annealed at 1200 °C in air and cooled in vacuum have the worst thermal stability due to the uneven particle size distribution.

4. All samples show excellent frequent stability below 1 MHz. The samples annealed at 950 °C in air have the largest cut-off frequency which is higher than 220 MHz.

Sintering conditions have a great impact on material properties. More work about controlling the annealing atmosphere needs to be done to obtain materials with high permeability and thermal stability at the same time.

Acknowledgements

This work was supported by National Natural Science Foundation of China (51962016) ; Fundamental Research Funds for the Central Universities of Civil Aviation University of China (3122021123)

Author contributions

Jun Wang contributed to experiment, measurement of data. Liling Zhou helped in data analysis and checking the figures.

Funding

National Natural Science Foundation of China, 51962016, xueyun zhou, Fundamental Research Funds for the Central Universities of Civil Aviation University of China, 3122021123, xueyun zhou

Data availability

The datasets generated during and/or analyzed during the current study are available from the corresponding author on reasonable request.

Declarations

Conflict of interest The authors declare that they have no known competing financial interests.

References

1. Hu. Jiyu, X. Liu, X. Kan, S. Feng, C. Liu, W. Wang, K.M.U. Rehman, M. Shazed, S. Zhou, Wu. Qiuyue, Characterization of texture and magnetic properties of Ni0.5Zn0.5TixFe2-xO4 spinel ferrites. J. Magn. Magn. Mater. **489**, 165411 (2019)
2. C. Beatrice, S. Dobák, V. Tsakaloudi, F. Fiorillo, A. Manioudaki, V. Zaspalis, Magnetic aging in TiO_2-doped Mn-Zn ferrites. J. Magn. Magn. Mater. **502**, 166576 (2020)
3. Wu. Guohua, Yu. Zhong, Ke. Sun, R. Guo, H. Zhang, X. Jiang, Wu. Chuanjian, Z. Lan, Ultra-low core losses at high frequencies and temperatures in MnZn ferrites with nano-$BatiO_3$ additives. J. Alloy. Compd. **821**, 153573 (2020)
4. A. Hussain, G. Bai, H. Huo, S. Yi, X. Wang, X. Fan, Mi. Yan, Co_2O_3 and SnO_2 doped MnZn ferrites for applications at 3–5MHz frequencies. Ceram. Int. **45**, 12544 (2019)
5. S.V. Bhandare, R. Kumar, A.V. Anupama, H.K. Choudhary, V.M. Jali, B., Sahoo, "mechanistic insights into the sol-gel synthesis of complex (quaternary) Co-Mn-Zn-spinel ferrites: an annealing dependent study." Ceram. Int. **46**, 17400 (2020)
6. Xu. Zhanyuan, J. Fan, T. Liu, S. Zhao, H. Zhang, F. Yin, T.L. YongHan, Microstructure and magnetic properies of MnZn ferrite powders prepared by nano-in-situ composite method. J. Alloy. Compd. **835**, 155285 (2020)
7. S. Mallesh, V. Srinivas, A comprehensive study on thermal stability and magnetic properties of MnZn-ferrite nanoparticles. J. Magn. Magn. Mater. **475**, 290 (2019)
8. JinAh Hwang, M. Choi, H.-S. Shin, Ju. Byeong-Kwon, MyoungPyo Chun, Structural and magnetic properties of

NiZn ferrite nanoparticles synthesized by a thermal decomposition method. Appl. Sci. **10**, 6279 (2020)
9. U.B. Gawas, V.M.S. Verenkar, V.T. Vader, A. Jain, S.S. Meen, Effects of sintering temperature on microstructure, initial permeability and electric behaviour of Ni-Mn-Zn ferrites. Mater. Chem. Phys. **275**, 125250 (2022)
10. M. Mahdiani, A. Sobhani, F. Ansari, M. Salavati-Niasari, Lead hexaferrite nanostructures: green amino acid sol–gel auto-combustion synthesis, characterization and considering magnetic property. J. Mater. Sci.: Mater. Electron. **28**, 17627 (2017)
11. Z. Xueyun, Z. Yuxiu, Z. Liling, Wu. Wei Jianning, D.Y. Junqing, Effect of Gd and La doping on the structure, optical and magnetic properties of NiZnCo ferrites. Ceram. Int. **45**, 6236 (2019)
12. P.P. Gauns, V.M.S. Dessai, Verenkar, Synthesis and characterization of Ni0.7−xMnxZn0.3Fe2 (C4H2O4)3·6N2H4 (x = 0.1–0.6): a precursor for the synthesis of nickel–manganese–zinc ferrites. J. Therm. Anal. Calorim. **142**, 1399 (2020)
13. Z. Duan, H. Chen, X. Tao, H. Mi, S. Lou, Xu. Ju, Fabrication and properties of MnZn ferrite with large length-diameter ratio. Ferroelectrics **554**, 204 (2020)
14. C. Murugesan, K. Ugendar, L. Okrasa, G. Jun Shen, Chandrasekaran, Zinc substitution effect on the structural, spectroscopic and electrical properties of nanocrystalline $MnFe_2O_4$ spinel ferrite. Ceram. Int. **47**, 1672 (2021)
15. J. Bennet, R. Tholkappiyan, K. Vishista, N. VictorJaya, Fathalla Hamed, Attestation in self-propagating combustion approach of spinel AFe_2O_4 (A = Co, Mg and Mn) complexes bearing mixed oxidation states: magnetostructural properties. Appl. Surf. Sci. **383**, 113 (2016)
16. W. Wang, A. Sun, X. Zhao, X. Pan, Y. Han, N. Suo, Yu. Lichao, Zhuo zuo, "structural and magnetic properties of Ni-Cu-Co ferrites prepared from sol-gel auto combustion method with different complexing agents." J. Alloy. Compd. **816**, 152501 (2020)
17. R.V. Parthasarathi Bera, B.H.P. Lakshmi, K. Tiwari, A. Shukla, A.K. Kundu, K. Biswas, H.C. Barshilia, Solution combustion synthesis, characterization, magnetic, and dielectric properites of CoFe2O4 and Co0.5M0.5-Fe2O4(M=Mn, Ni, and Zn). Phys. Chem. Chem. Phys **22**, 20087 (2020)
18. L. Gao, Z. Liu, Z. Yang, L. Cao, C. Feng, M. Chua, J. Tang, Synthesis and magnetism property of manganese ferrite $MnFe_2O_4$ by selective reduction and oxidization roasting process. Appl. Surf. Sci. **508**, 145292 (2020)
19. S. Liu, L. Wang, K. Chou, Synthesis of metal-doped Mn-Zn ferrite from the leaching solutions of vanadium slag using hydrothermal method. J. Magn. Magn. Mater. **449**, 49 (2018)
20. L. George, C. Viji, M. Maheen, E.M. Mohammed, Enhanced magnetic properties at low temperature of Mn substituted Ni-Zn mixed ferrite doped with Gd ions for magnetoresistive applications. Mater. Res. Bull. **126**, 110833 (2020)
21. N.I. Abu-Elsaad, S.A. Mazen, H.M. Salem, The effect of zinc substitution and heat treatment on microstructural and magnetic properties of Li ferrite nanoparticles. J. Alloy. Compd. **835**, 155227 (2020)
22. P. Liu, Z. Yao, J. Zhou, Z. Yang, L.B. Kong, Small magnetic Co-doped NiZn ferrite/graphene nanocomposites and their dual-region microwave absorption performance. J. Mater. Chem. C **4**, 9738 (2016)
23. Y. Mouhib, M. Belaiche, M. Elansary, C.A. Ferdi, Effect of heating temperature on structural and magnetic properties of zinc ferrite nanoparticles synthesized for the first time in presence of Moroccan reagents. J. Alloy. Compd. **895**, 162634 (2022)
24. G.M. Shweta, L.R. Naik, R.B. Pujar, S.N. Mathad, Influence of magnesium doping on structural and elastic parameters of Nickel Zinc nanoferrites. Mater. Chem. Phys. **257**, 123825 (2021)
25. Wu. Xiao-Hui, Z.-X. Tao, L.-Z. Li, Wu. Chong-Sheng, X.-X. Zhong, R. Wang, P.-C. Xiang, K.-L. Li, N. Lin, Crystal structure and enhanced magneto-electric properties of cobalt-substituted nickel-zinc ferrite. J. Mater. Sci: Mater. Electron. **31**, 20277 (2021)
26. Z.Q. Liu, Z.G. Peng, C.C. Lv, X.L. Fu, Doping effect of Sm^{3+} on magnetic and dielectric properties of Ni-Zn ferrites. Ceram. Int. **43**, 1449 (2017)
27. L. Néel, Propriétés magnétiques des ferrites; ferrimagnétisme et anti-ferromagnétisme. Ann. Phys. **3**, 137e198 (1948)
28. R.S. Yadav, I. Kuřitka, J. Vilcakova, J. Havlica, J. Masilko, L. Kalina, J. Tkacz, V. Enev, M. Hajdúchová, Structural, magnetic, dielectric, and electrical properties of NiFe2O4 spinel ferrite nanoparticles prepared by honey-mediated sol-gel combustion. J. Phys. Chem. Solids. **107**, 150 (2017)
29. T. Jahanbin, M. Hashim, K. Amin Mantori, Comparative studies on the structure and electromagnetic properties of Ni-Zn ferrites prepared via co-precipitation and conventional ceramic processing routes. J. Magn. Magn. Mater. **322**, 2684 (2010)
30. S. Ikram, J. Jacob, M.I. Arshad, K. Mahmood, A. Ali, N. Sabir, N. Amin, S. Hussain, Tailoring the structural, magnetic and dielectric properties of Ni-$ZnCdFe_2O_4$ spinel ferrites by the substitution of lanthanum ions. Ceram. Int. **45**(3), 3563 (2019)
31. X. Zhou, J. Wang, L. Zhou, D. Yao, Structure, magnetic and microwave absorption properties of NiZnMn ferrite ceramics. J. Magn. Magn. Mater. **534**, 168043 (2021)

32. K. Jiang, K. Li, C. Peng, Y. Zhu, Effect of multi-additives on the microstructure and magnetic properties of high permeability Mn-Zn ferrite. J. Alloy. Compd. **541**, 472 (2012)
33. A.K.M. Akther Hossain, T.S. Biswas, S.T. Mahmud, T. Yanagida, H. Tanaka, T. Kawai, Enhancement of initial permeability due to Mn substitution in polycrystalline Ni0.5-xMnxZn0.5Fe2O4. J. Magn. Magn. Mater. **321**, 81 (2009)
34. E. Rezlescu, L. Sachelarie, P.D. Popa, N. Rezlescu, Effect of substitution of divalent ions on the electrical and magnetic properties of Ni–Zn–Me ferrites. IEEE Trans. Magn. **36**, 3962 (2000)
35. Z. Yue, Ji. Zhou, X. Wang, Z. Gui, L. Li, Preparation and magnetic properties of titanium-substituted LiZn ferrites via a sol-gel auto-combustion process. J. Eur. Ceram. Soc. **23**, 189 (2003)
36. S.E. Shirsath, B.G. Toksha, R.H. Kadam, S.M. Patange, D.R. Mane, G.S. Jangam, A. Ghasemi, Doping effect of Mn^{2+} on the magnetic behavior in Ni–Zn ferrite nanoparticles prepared by sol–gel auto-combustion. J. Phys. Chem. Solids. **71**, 1669 (2010)